



Pt–WO_x on monoclinic or tetrahedral ZrO₂: Crystal phase effect of zirconia on glycerol hydrogenolysis to 1,3-propanediol

Yiqiu Fan^a, Shijie Cheng^a, Hao Wang^a, Jing Tian^a, Songhai Xie^a, Yan Pei^a,
Minghua Qiao^{a,*}, Baoning Zong^{b,*}

^a Collaborative Innovation Center of Chemistry for Energy Materials, Department of Chemistry and Shanghai Key Laboratory of Molecular Catalysis and Innovative Materials, Fudan University, Shanghai 200433, PR China

^b State Key Laboratory of Catalytic Materials and Chemical Engineering, Research Institute of Petroleum Processing, SINOPEC, Beijing 100083, PR China

ARTICLE INFO

Article history:

Received 25 March 2017

Received in revised form 25 May 2017

Accepted 3 June 2017

Available online 6 June 2017

Keywords:

glycerol hydrogenolysis

1,3-propanediol

ZrO₂

Crystal phase

Pt–WO_x

ABSTRACT

The effects of the crystal phases of ZrO₂ in the Pt–WO_x/ZrO₂ catalysts on glycerol hydrogenolysis to 1,3-propanediol (1,3-PDO) were comparatively studied. Pt and WO_x were sequentially deposited on monoclinic (*m*-ZrO₂) and tetragonal (*t*-ZrO₂) ZrO₂ supports with similar surface areas by the wetness impregnation method. On both catalysts, sub-nanosized Pt particles were well dispersed on the supports, and the WO_x species were mainly in the monomeric state and partly covered the Pt particles. The Pt–WO_x/*m*-ZrO₂ catalyst had larger Pt particle size and less Brønsted acid sites than the Pt–WO_x/*t*-ZrO₂ catalyst. In glycerol hydrogenolysis, the glycerol conversion and 1,3-PDO selectivity on the Pt–WO_x/*m*-ZrO₂ catalyst were less than one half of those on the Pt–WO_x/*t*-ZrO₂ catalyst. The Pt–WO_x/*t*-ZrO₂ catalyst exhibited a high 1,3-PDO yield of 49.4%, an excellent 1,3-PDO productivity of 5.10 g g_{Pt}^{−1} h^{−1}, and good recyclability. The superiority of the Pt–WO_x/*t*-ZrO₂ catalyst in glycerol hydrogenolysis to 1,3-PDO is attributed to the better synergy between smaller Pt particles in affording hydrogen atoms and more Brønsted acid sites in converting glycerol to the intermediate suitable for the formation of 1,3-PDO.

© 2017 Elsevier B.V. All rights reserved.

1. Introduction

Highly functionalized biomass-derived glycerol is a versatile platform molecule for the production of a variety of useful commodity chemicals [1–4]. 1,3-PDO is one of the most value-added derivatives from glycerol in that it is an important chemical for the manufacture of polytriethylene terephthalate, polyurethanes, and cyclic compounds with wide applications [1]. Hence, many catalyst systems have been designed to produce 1,3-PDO through the glycerol hydrogenolysis route [5–7], which represents a highly environmentally sustainable and efficient alternative to the traditional petrochemical routes such as hydroformylation of ethylene oxide and hydration of acrolein [8] and the tedious biochemical routes such as fermentation of glycerol [9]. Currently, a general consensus is that an efficacious catalyst for glycerol hydrogenolysis to 1,3-PDO is composed of a noble metal such as Pt or Ir at least for the activation of H₂, an oxophilic promoter such as SO₄^{2−}, ReO_x, or WO_x for the selective activation of the secondary hydroxyl group,

and an oxide support for the dispersion of these active components [5,6].

Recently, the Pt–WO_x-based catalysts have attracted enormous interests in that they possess lower causticity to the reactor than the SO₄^{2−}-promoted catalysts and lower catalyst cost than the ReO_x-promoted catalysts [10]. It was identified that the catalytic performances of the Pt–WO_x-based catalysts are closely associated with the type of the oxide support. Kurosaka et al. found that among the Al–MCM-41, SiO₂–Al₂O₃, Al₂O₃, anatase TiO₂, zeolite H-Y, and ZrO₂ supports, the Pt/WO₃/ZrO₂ catalyst displayed the highest 1,3-PDO selectivity of 24.2% at glycerol conversion of 85.8% with 1,3-dimethyl-2-imidazolidinone (DMI) as the solvent [11]. Subsequently, Gong et al. acquired the 1,3-PDO selectivity of 29.3% at glycerol conversion of 45.6% over a similar Pt/WO₃/ZrO₂ catalyst using a mixture of DMI and ethanol as the solvent [12]. Referring to the X-ray diffraction (XRD) pattern [11], the ZrO₂ support in those works is a composite of *m*-ZrO₂ and *t*-ZrO₂. Qin et al. reported the 1,3-PDO selectivity of 45.6% at glycerol conversion of 70.2% over the Pt/WO₃/ZrO₂ catalyst without addressing the crystallographic form of ZrO₂ [13]. Zhu et al. reported the 1,3-PDO selectivity of 48.1% at glycerol conversion of 24.1% over the Pt–H₄SiW₁₂O₄₀/ZrO₂ catalyst [14]. Over the Li-modified Pt–H₄SiW₁₂O₄₀/ZrO₂ catalyst, they obtained the 1,3-PDO selectivity of 53.6% at glycerol conversion

* Corresponding authors.

E-mail addresses: mhqiao@fudan.edu.cn (M. Qiao), zongbn.ripp@sinopec.com (B. Zong).

of 43.5% [15]. In those two catalysts, the ZrO_2 support was monoclinic. The same group modified the $\text{Pt}/\text{WO}_x/\text{ZrO}_2$ catalyst with 2.5–10 wt% of SiO_2 ($x\text{Pt}/\text{WO}_x/\text{ZrSi}$) by deposition–precipitation of SiO_2 with ZrO_2 and obtained the 1,3-PDO selectivity of 52.0% at glycerol conversion of 54.3% over the catalyst with 5.0 wt% of SiO_2 [16]. In the optimal $5\text{Pt}/\text{WO}_x/\text{ZrSi}$ catalyst, however, ZrO_2 was mainly in the form of tetrahedral. Surprisingly, there is no detailed study about the effects of the crystal phases of ZrO_2 on this reaction, which will shed light on the rational design of more effective catalysts for glycerol hydrogenolysis to 1,3-PDO.

For crystalline ZrO_2 , there are three polymorphs: m - ZrO_2 , t - ZrO_2 , and cubic ZrO_2 (c - ZrO_2) [17]. Because of its extremely high crystallization temperature (2643 K) and hence extremely low specific surface area (S_{BET}), c - ZrO_2 is rarely used as the catalyst support. The crystal phase of ZrO_2 is highly relevant to the catalytic activity and/or selectivity in a wide range of reactions. For instance, in acid-catalyzed n -alkane isomerization, Stichert reported that sulfated m - ZrO_2 is less active than sulfated t - ZrO_2 by a factor of about four [18]. For the synthesis of higher alcohols from syngas, the Pd/t - ZrO_2 catalyst exhibited a high activity to the formation of ethanol, while the Pd/m - ZrO_2 catalyst exhibited a high activity to the formation of isobutanol [19]. For methanol synthesis from CO hydrogenation, the Cu/t - ZrO_2 catalyst showed higher activity than the amorphous and monoclinic ZrO_2 -supported ones [20]. In liquid-phase hydrogenation of benzene, the $\text{Ru}-\text{B}/t$ - ZrO_2 catalyst was more selective towards cyclohexene than the amorphous and monoclinic ZrO_2 -supported counterparts [21]. In the water–gas shift (WGS) reaction, the rate of per mole of surface Pt on the Pt/t - ZrO_2 catalyst was about five times higher than that on the Pt/m - ZrO_2 catalyst [22]. In partial oxidation of methane, the Rh/t - ZrO_2 catalyst was far more active and selective than the Rh/m - ZrO_2 catalyst [23]. However, in low-temperature WGS reaction, the Au/m - ZrO_2 catalyst showed much higher activity than the Au/t - ZrO_2 catalyst [24]. In alkylation of phenol, the $\text{V}_2\text{O}_5/m$ - ZrO_2 catalyst was also about four times more active than the $\text{V}_2\text{O}_5/t$ - ZrO_2 catalyst [25]. Therefore, we anticipate that the crystal phase effect of ZrO_2 will also play a significant role in glycerol hydrogenolysis to 1,3-PDO over the $\text{Pt}-\text{WO}_x/\text{ZrO}_2$ catalysts.

Herein, we synthesized the m - ZrO_2 and t - ZrO_2 supports with similar S_{BET} by means of the hydrothermal method and the precipitation method, respectively, to concentrate on the crystal phase effect. We revealed that despite of the same Pt and WO_x loadings and preparation procedures, the $\text{Pt}-\text{WO}_x/t$ - ZrO_2 catalyst was far more active and selective towards 1,3-PDO than the $\text{Pt}-\text{WO}_x/m$ - ZrO_2 catalyst in aqueous-phase hydrogenolysis of glycerol. The pronounced crystal phase effects of ZrO_2 were interpreted on the basis of detailed characterization results and control experiments. This work demonstrates for the first time the importance of employing a suitable crystal phase of ZrO_2 in the rational development of a supported catalyst for glycerol hydrogenolysis to 1,3-PDO.

2. Experimental

2.1. Preparation

The chemicals were of analytical grade (A. R.) and commercially available from Sinopharm Chemical Reagent and used without further purification. Deionized water was used throughout the experiments. The gases were commercially available from Shanghai Youjiali Liquid Helium.

By comprehensively consulting the synthetic strategies and making necessary modifications, we successfully synthesized the m - ZrO_2 and t - ZrO_2 supports with similar S_{BET} of 118 and $122 \text{ m}^2 \text{ g}^{-1}$, respectively (Table 1), hence the possible interference

of the discrepancy in S_{BET} with the crystal phase effects can be excluded. The m - ZrO_2 support was synthesized by the hydrothermal method adapted from that proposed by Li et al. [26]. Namely, 7.40 g of zirconyl nitrate dihydrate and 19.22 g of urea were dissolved in 80 ml of deionized water under stirring, which was then transferred to a 100 ml-capacity Teflon-lined stainless-steel autoclave. After hydrothermal treatment at 433 K for 20 h, the resulting solids were filtered off, washed with deionized water, dried at 373 K overnight, and calcined in static air at 673 K for 4 h with a heating rate of 2 K min^{-1} .

The t - ZrO_2 support was synthesized according to the precipitation method raised by Jung and Bell [27]. Namely, 24.17 g of zirconium oxychloride octahydrate was dissolved in 150 ml of deionized water under stirring, to which 50 ml of 14.8 M ammonium hydroxide was added dropwise. The solution was kept at room temperature for 3 h and then heated to 373 K for 48 h under stirring. The precipitates were immediately filtered off, washed with deionized water repeatedly to remove residual chloride ions as confirmed by silver nitrate test, dried at 383 K overnight, and calcined in static air at 873 K for 5 h with a heating rate of 10 K min^{-1} .

The $\text{Pt}-\text{WO}_x/m$ - ZrO_2 and $\text{Pt}-\text{WO}_x/t$ - ZrO_2 catalysts were prepared by means of a two-step impregnation method. First, the Pt/ZrO_2 catalysts were prepared by impregnating 0.50 g of the as-synthesized ZrO_2 supports with 2.65 ml of 1.93 mM chloroplatinic acid hexahydrate aqueous solution at 333 K for 3 h under gentle stirring. The suspension was evaporated at 393 K overnight and calcined at 723 K in static air for 4 h with a heating rate of 5 K min^{-1} . Second, 0.50 g of the as-prepared Pt/ZrO_2 catalysts were impregnated with 5.0 ml of 10.0 g l^{-1} silicotungstic acid ($\text{H}_4\text{SiW}_{12}\text{O}_{40} \cdot x\text{H}_2\text{O}$, HSiW) aqueous solution at 333 K for 3 h under gentle stirring, followed by evaporation at 393 K overnight. The solids were further calcined at 723 K in static air for 4 h with a heating rate of 5 K min^{-1} and then reduced in 5 vol% H_2/Ar flow (100 ml min^{-1}) at 573 K for 2 h with a heating rate of 2 K min^{-1} to obtain the $\text{Pt}-\text{WO}_x/\text{ZrO}_2$ catalysts. The nominal loadings of Pt and W were 2.0 wt% and 7.7 wt%, respectively. Due to the relatively low W loading and the high W/Si stoichiometry of 12 in HSiW, the nominal Si loading was 0.097 wt%, so the influence of Si on the catalytic performance should be negligible.

2.2. Characterization

The multi-point S_{BET} was measured by N_2 physisorption at 77 K on a Micromeritics Quadra apparatus. The sample was loaded in a glass adsorption tube and pretreated at 523 K under flowing N_2 for 3 h. The bulk composition of the catalyst was determined by the inductively coupled plasma-atomic emission spectroscopy (ICP-AES; Thermo Elemental IRIS Intrepid).

The XRD pattern was acquired on a Bruker AXS D8 Advance X-ray diffractometer using Ni-filtered $\text{Cu K}\alpha$ radiation ($\lambda = 0.15418 \text{ nm}$) equipped with a LynxEye 1-dimensional linear Si strip detector. The tube voltage was 40 kV, and the current was 40 mA. The 2θ angles were scanned from 10° to 80° at 5° min^{-1} with a step size of 0.02° .

The Raman spectrum was recorded at room temperature on a Horiba Jobin Yvon XploRA Raman spectrometer at an excitation wavelength of 532 nm using a 12.5 mW He–Ne laser source. The spectral resolution was ca. 1.8 cm^{-1} .

CO chemisorption was conducted on a Micromeritics 2750 chemisorption apparatus equipped with a thermal conductivity detector (TCD). The weighed catalyst ($\sim 50 \text{ mg}$) was reduced at 573 K for 3 h in 5 vol% H_2/Ar flow (25 ml min^{-1}), purged with He at 473 K for 2 h, and then cooled down to 298 K. Pure CO pulses were injected until the eluted peak did not change in intensity [28]. The CO/Pt adsorption stoichiometry of 1 was assumed when calculat-

Table 1Basic physicochemical properties of the as-synthesized *m*-ZrO₂, *t*-ZrO₂, and the Pt-WO_x/*m*-ZrO₂ and Pt-WO_x/*t*-ZrO₂ catalysts.

Sample	Pt loading ^a (wt%)	W loading ^a (wt%)	Si loading (wt%)	W surface density (atom nm ⁻²)	<i>S</i> _{BET} ^b (m ² g ⁻¹)	<i>V</i> _{pore} ^b (cm ³ g ⁻¹)	<i>d</i> _{pore} ^b (nm)	<i>D</i> _{Pt} ^c (%)	<i>S</i> _{Pt} ^c (m ² g ⁻¹)	<i>d</i> _{Pt} ^c (nm)
<i>m</i> -ZrO ₂	/	/	/	/	118	0.28	11.2	/	/	/
<i>t</i> -ZrO ₂	/	/	/	/	122	0.39	11.0	/	/	/
Pt-WO _x / <i>m</i> -ZrO ₂	1.91	7.50	0.095	2.45	100	0.23	11.2	32	79	3.5
Pt-WO _x / <i>t</i> -ZrO ₂	1.94	7.56	0.093	2.36	105	0.33	10.6	53	131	2.1

^a Determined by ICP-AES.^b Specific surface area, pore volume, and pore size determined by N₂ physisorption.^c Dispersion, active surface area, and particle size of Pt determined by CO chemisorption.

ing the dispersion (*D*_{Pt}), active surface area (*S*_{Pt}), and particle size of Pt [29].

High-resolution transmission electron microscopic (HRTEM) image and high-angle annular dark field (HAADF) image were observed on a Tecnai G² S-Twin F20 field-emission (S)TEM microscope operated at 200 kV. The catalyst was ground in an agate mortar, dispersed in anhydrous ethanol, and dripped onto a carbon film-coated copper grid. More than 200 particles were measured to construct the particle size distribution (PSD) histogram.

Ultraviolet–visible diffuse reflectance spectrum (UV-vis DRS) was collected on a Perkin-Elmer Lambda650 s spectrometer from 200 to 800 nm with a step size of 0.2 nm. BaSO₄ was taken as a reference to record the data points.

Fourier-transform infrared spectroscopy (FTIR) was conducted on a Nicolet Nexus 470 IR spectrometer equipped with a deuterated triglycine sulfate (DTGS) detector. The sample was finely ground, evenly mixed with KBr with a mass ratio of 1/20, and pelletized. The spectral resolution was 4 cm⁻¹, and 32 scans were recorded for each spectrum.

For pyridine-adsorption FTIR (Py-IR), about 20 mg of the sample was pressed into a self-supporting wafer of 2 cm in diameter. The wafer was loaded in an IR cell with CaF₂ windows, evacuated at 573 K for 1 h, and then exposed to the pyridine vapor after being cooled down to 303 K. The spectra were recorded at 373 and 473 K after evacuation for 30 min to eliminate the influence of the hydrogen-bonded and physically adsorbed pyridine [30]. Quantitative analyses of Lewis acid sites and Brønsted acid sites were based on the integrated areas of the adsorption bands at ca. 1448 and 1542 cm⁻¹, respectively. The corresponding extinction coefficients were referred to the work of Emeis [31].

X-ray photoelectron spectroscopy (XPS) was carried out on a Kratos AXIS-Ultra spectrometer using Al Kα radiation (*hν* = 1486.6 eV) as the excitation source. The catalyst was evacuated in the pretreatment chamber at 298 K overnight, and then transferred to the analyzing chamber with the background pressure below 2 × 10⁻⁹ Torr. All binding energy (BE) values were referenced to the Zr 3d_{5/2} BE of ZrO₂ at 182.2 eV with an accuracy of ± 0.2 eV.

Temperature-programmed desorption of H₂ (H₂-TPD) was carried out on the same apparatus as CO chemisorption. About 50 mg of the catalyst was placed in a quartz tube and reduced at 573 K for 3 h in 5 vol% H₂/Ar flow (25 ml min⁻¹). After being cooled down to 323 K, pure H₂ pulses were injected until the eluted peak did not change in intensity. The catalyst was then purged by pure Ar until the signal returned to the baseline. The desorption profile was acquired by heating the catalyst in Ar from 323 to 900 K at a ramping rate of 10 K min⁻¹.

2.3. Catalytic testing

The aqueous-phase hydrogenolysis of glycerol was performed on a 10 ml-capacity Teflon-lined stainless steel autoclave, in which 100 mg of catalyst and 2.0 g of 30 wt% glycerol aqueous solution

were charged. The concentration of glycerol followed that of crude glycerol [32]. The autoclave was sealed and purged with H₂ six times to expel air. During the reaction, the temperature was kept at 413 K, the H₂ pressure was 8.0 MPa, and the stirring rate was 500 rpm. After reaction, the liquid phase was analyzed on a GC-9560 gas chromatograph fitted with an HP-INNO Wax column (30 m × 0.32 mm × 0.50 μm) and a flame ionization detector (FID), using butanol and 1,4-butanediol as internal standards. The liquid products were also qualified by gas chromatography-mass spectrometry (GC-MS, Finnigan Voyager) using an identical HP-INNO Wax column. The gas phase was detected on a GC-9560 gas chromatograph fitted with a 2 m-long TDX-01 packed stainless steel column connected to a TCD and on a GC-9160 gas chromatograph fitted with a PONA capillary column (50 m × 0.25 mm × 0.50 μm) connected to an FID. Propane was identified as the only carbon-containing gaseous product.

On the basis of the chromatographic results, the conversion of glycerol was calculated as: Conversion = (initial moles of glycerol – moles of glycerol after reaction)/(initial moles of glycerol) × 100%.

The conversion of glycerol to liquid products (CTL) was calculated as: CTL = (total moles of C in liquid products)/(initial moles of C in glycerol × Conversion) × 100%.

The selectivity to a specific liquid product (Sel.) was calculated as: Sel. = (moles of C in a specific liquid product/moles of C in all liquid products) × 100%.

The yield of 1,3-PDO (Yield_{1,3-PDO}) was calculated as: Yield_{1,3-PDO} = (CTL × Sel. to 1,3-PDO) × 100%.

The space–time yield (STY) of 1,3-PDO was calculated as: STY = (Initial moles of glycerol × Yield_{1,3-PDO} × 76)/(catalyst weight × Pt loading × reaction time).

3. Results

3.1. Validation of the crystal phase of the as-synthesized ZrO₂

XRD and Raman techniques were employed to validate the successful synthesis of the phase-pure *m*-ZrO₂ and *t*-ZrO₂ supports. The XRD patterns in Fig. 1 show that the as-synthesized *m*-ZrO₂ only exhibited characteristic diffraction peaks of monoclinic ZrO₂ (JCPDS 37–1484), whereas the as-synthesized *t*-ZrO₂ exhibited diffraction peaks exclusively from tetragonal ZrO₂ (JCPDS 50–1089). The average crystallite sizes of *m*-ZrO₂ and *t*-ZrO₂ were estimated by the Scherrer formula from the broadening of the most intensive (111) peak at 28.3° and the (011) peak at 30.2°, respectively. It turned out that the crystallite sizes were 7.5 nm for *m*-ZrO₂ and 8.1 nm for *t*-ZrO₂. Although *m*-ZrO₂ is the favored crystal phase for ZrO₂ at temperatures below 1443 K, it is known that *t*-ZrO₂ can be stabilized at room temperature by a crystallite size effect when the size is smaller than 10 nm [33].

The Raman spectra in Fig. 2 show that the as-synthesized *m*-ZrO₂ only displayed bands at 217, 303, 333, 379, 478, 534, 557, 613, and 626 cm⁻¹ due to monoclinic ZrO₂ [34,35], whereas the

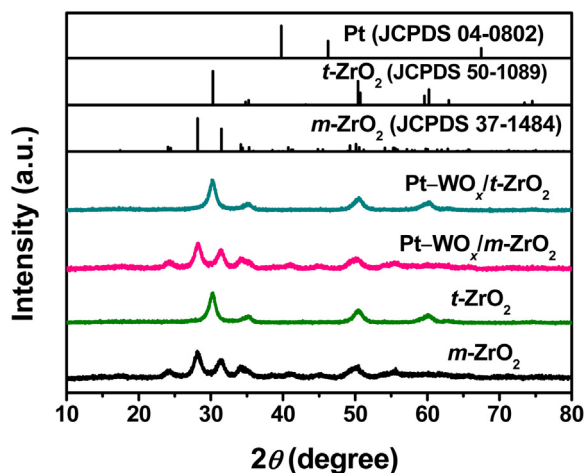


Fig. 1. The XRD patterns of the as-synthesized *m*-ZrO₂, *t*-ZrO₂, and the Pt-WO_x/*m*-ZrO₂ and Pt-WO_x/*t*-ZrO₂ catalysts.

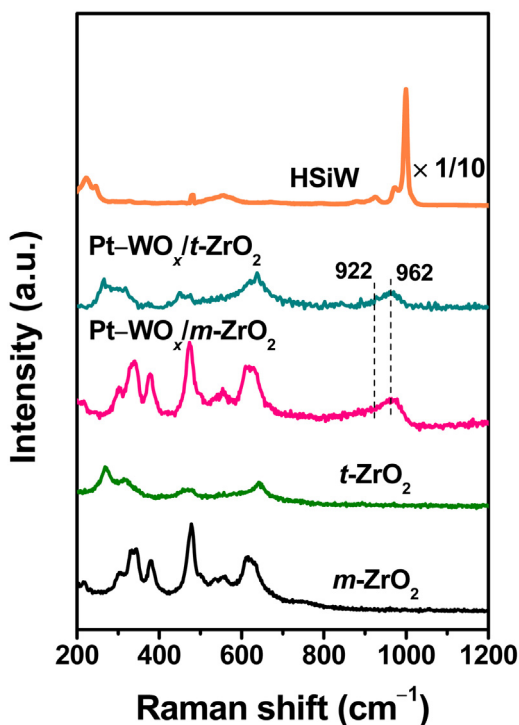


Fig. 2. The Raman spectra of the as-synthesized *m*-ZrO₂, *t*-ZrO₂, and the Pt-WO_x/*m*-ZrO₂ and Pt-WO_x/*t*-ZrO₂ catalysts. The Raman spectrum of HSiW is also shown for reference.

as-synthesized *t*-ZrO₂ only displayed bands at 271, 316, 460, 475, and 644 cm⁻¹ ascribable to tetrahedral ZrO₂ [34,36]. Since XRD is a bulk-specific technique, while Raman is surface sensitive [37], their combination convincingly verifies that the bulk and surface of the as-synthesized *m*-ZrO₂ and *t*-ZrO₂ are uniform in crystal structure.

3.2. Characterization of the Pt-WO_x/ZrO₂ catalysts

3.2.1. Bulk composition and textural property

Fig. S1 presents the N₂ adsorption–desorption isotherms of the as-synthesized ZrO₂ supports and the Pt-WO_x/ZrO₂ catalysts. The appearance of the type IV isotherms with H3 hysteresis loops indicated the presence of the plate-like mesopores in the as-synthesized ZrO₂ supports as well as in the Pt-WO_x/ZrO₂ catalysts by stacking of the ZrO₂ crystals. Analogous to the as-synthesized

ZrO₂ supports, the Pt-WO_x/*m*-ZrO₂ and Pt-WO_x/*t*-ZrO₂ catalysts also displayed identical *S*_{BET} values (Table 1). As also listed in Table 1, the practical Pt and W loadings on the Pt-WO_x/ZrO₂ catalysts agreed well with the nominal loadings. In addition, the practical Si loadings on both catalysts were around 0.094 wt%, which were also close to the nominal Si loading.

Albeit their identical Pt loading and *S*_{BET}, CO chemisorption revealed that there were pronounced disparities in the *D*_{Pt} and *S*_{Pt} between the Pt-WO_x/*m*-ZrO₂ catalyst and the Pt-WO_x/*t*-ZrO₂ catalyst (Table 1). For the Pt-WO_x/*m*-ZrO₂ catalyst, the *D*_{Pt} was 32%, and the *S*_{Pt} was 79 m² g_{Pt}⁻¹. For the Pt-WO_x/*t*-ZrO₂ catalyst, the *D*_{Pt} and *S*_{Pt} were drastically improved to 53% and 131 m² g_{Pt}⁻¹, respectively. In line with our finding, Campa et al. reported that the dispersion of Rh on the Rh/*t*-ZrO₂ catalyst was higher than that on the Rh/*m*-ZrO₂ catalyst [23]. Accordingly, the Pt particle size derived from CO chemisorption was 3.5 nm for the Pt-WO_x/*m*-ZrO₂ catalyst, which is much larger than the size of 2.1 nm on the Pt-WO_x/*t*-ZrO₂ catalyst, showing that the crystal phase of ZrO₂ imposed strong influence on the dispersion of Pt.

3.2.2. Phase composition

The XRD patterns of the Pt-WO_x/ZrO₂ catalysts are also shown in Fig. 1. Except for the diffractions from the ZrO₂ supports, both catalysts did not display any feature from the face-centered cubic (fcc) Pt, which is consistent with the low loading and small particle size of Pt. Moreover, the diffraction peaks due to crystalline WO₃ were also not available, inferring the high dispersion of the WO_x species. The surface density of the W atoms on the Pt-WO_x/*t*-ZrO₂ and Pt-WO_x/*m*-ZrO₂ catalysts were 2.36 and 2.45 W atom nm⁻², respectively. According to Iglesia and co-workers [38], the WO_x units with surface density of 0–4 W atom nm⁻² do not interact with each other to form the bridging W–O–W bonds of the polytungstate species, which accounts for the lacking of the diffractions from the WO_x species in our case.

3.2.3. Microstructure

The HRTEM images of the Pt-WO_x/ZrO₂ catalysts are presented as Fig. 3a and b. On the Pt-WO_x/*m*-ZrO₂ catalyst, we observed only the lattice fringes with interplanar distance of 3.16 Å due to the (111) planes of *m*-ZrO₂. Similarly, on the Pt-WO_x/*t*-ZrO₂ catalyst, there were only lattice fringes with interplanar distance of 2.94 Å due to the (011) planes of *t*-ZrO₂. These observations confirm again the preservation of the crystal phases of the ZrO₂ supports after the loading of Pt and WO_x. Besides, there are some dark-contrast, lattice fringe-free, and sub-nanosized particles attributable to Pt and WO_x, which is consistent with the failure in identifying these species by XRD. Statistics revealed that the mean sizes of the particles on the Pt-WO_x/*m*-ZrO₂ catalyst and the Pt-WO_x/*t*-ZrO₂ catalyst were as small as 0.72 ± 0.11 nm and 0.59 ± 0.07 nm, respectively. The HAADF–STEM images of the Pt-WO_x/ZrO₂ catalysts (Fig. 3c and d) substantiated the slightly larger particle size on the Pt-WO_x/*m*-ZrO₂ catalyst than on the Pt-WO_x/*t*-ZrO₂ catalyst. However, the closeness of the atomic numbers of Pt and W and the limitation of the resolution of the energy dispersive spectroscopy (EDS) for sub-nanosized particles impede a straightforward determination of the particle size of Pt. Therefore, we acquired the HRTEM images of the Pt/ZrO₂ catalysts without WO_x to gain insights into the particle sizes of Pt on the Pt-WO_x/ZrO₂ catalysts. As displayed in Fig. 3e and f, the particle sizes of Pt on the Pt/*m*-ZrO₂ catalyst and the Pt/*t*-ZrO₂ catalyst were 0.51 ± 0.05 nm and 0.41 ± 0.06 nm, respectively, implying a better dispersion of Pt on the Pt-WO_x/*t*-ZrO₂ catalyst than on the Pt-WO_x/*m*-ZrO₂ catalyst. It should be mentioned that in the TEM images of the Pt/*m*-ZrO₂ and Pt/*t*-ZrO₂ catalysts at a larger scale (Fig. S2), no larger Pt particles could be identified.

Interestingly, although CO chemisorption also indicated a better dispersion of Pt on the Pt-WO_x/*t*-ZrO₂ catalyst, the particle sizes

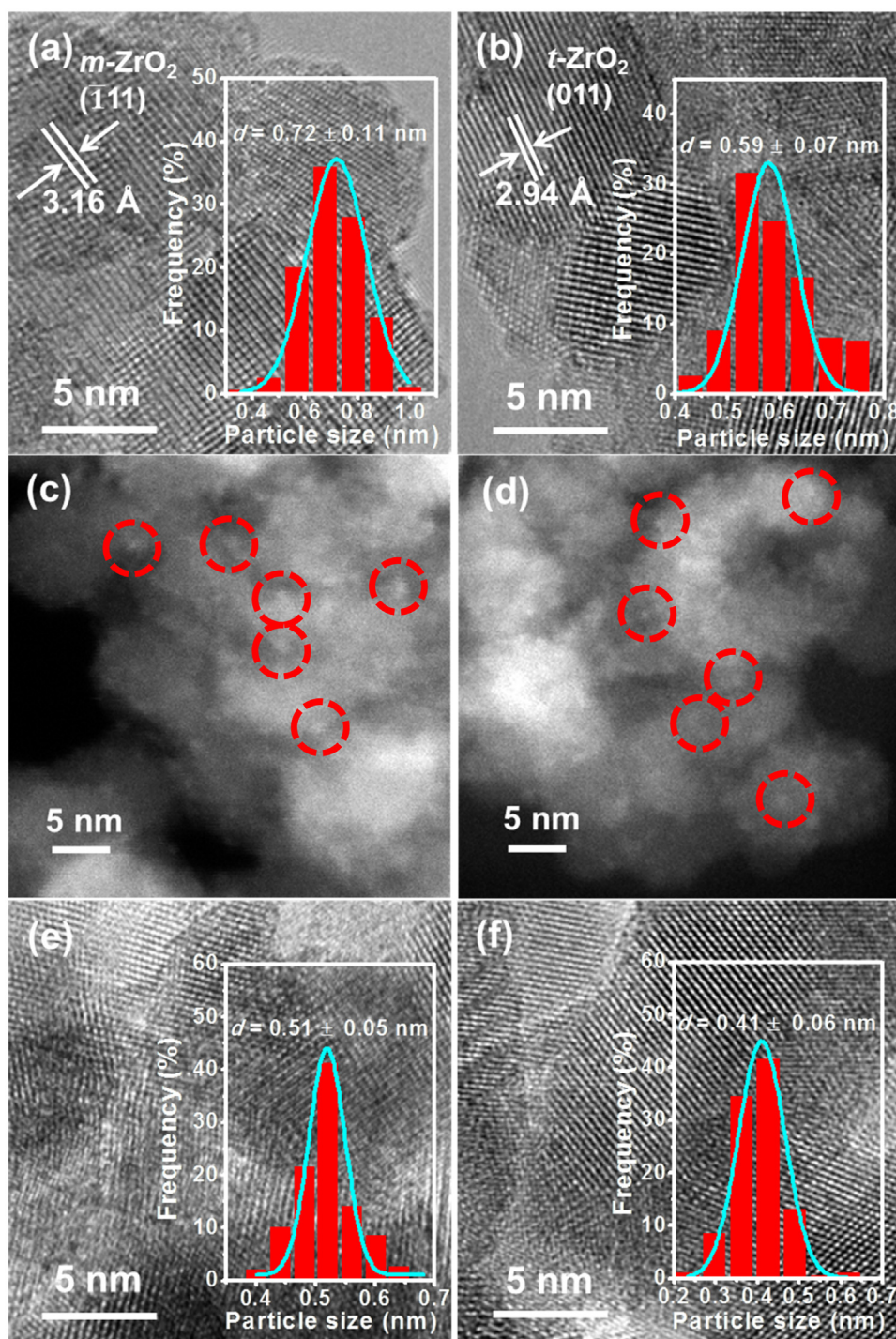


Fig. 3. The HRTEM images and particle size distribution histograms of the (a) Pt-WO_x/m-ZrO₂, (b) Pt-WO_x/t-ZrO₂, (e) Pt/m-ZrO₂, and (f) Pt/t-ZrO₂ catalysts. (c) and (d) are the HAADF-STEM images of the Pt-WO_x/m-ZrO₂ and Pt-WO_x/t-ZrO₂ catalysts, respectively.

of Pt derived from CO chemisorption were much larger than those determined by HRTEM. This discrepancy may be reconciled by the decoration of WO_x on the surface of the sub-nanosized Pt particles, considering that the Pt-WO_x/ZrO₂ catalysts were prepared by loading Pt first followed by WO_x, and the latter does not adsorb CO [10]. Therefore, the amount of CO adsorbed on the sub-nanosized Pt particles was reduced, leading to the particle sizes of Pt derived from CO chemisorption much larger than those measured by HRTEM. In addition, according to Kiely and co-workers, the dimension of one

WO_x unit is ca. 0.08 nm [39]. Hence, the ~0.2 nm enlargement of the particle diameters on the Pt-WO_x/ZrO₂ catalysts with respect to those on the WO_x-free Pt/ZrO₂ catalysts observed by HRTEM (Fig. 3) can be satisfactorily rationalized by surface decoration of the Pt particles by monomeric WO_x. In contrast, the particle sizes of Pt on the WO_x-free Pt/m-ZrO₂ and Pt/t-ZrO₂ catalysts measured by CO chemisorption were 1.0 and 0.7 nm, respectively, which deviated much less pronouncedly as compared to the Pt-WO_x/ZrO₂ catalysts from the Pt particle sizes determined by HRTEM.

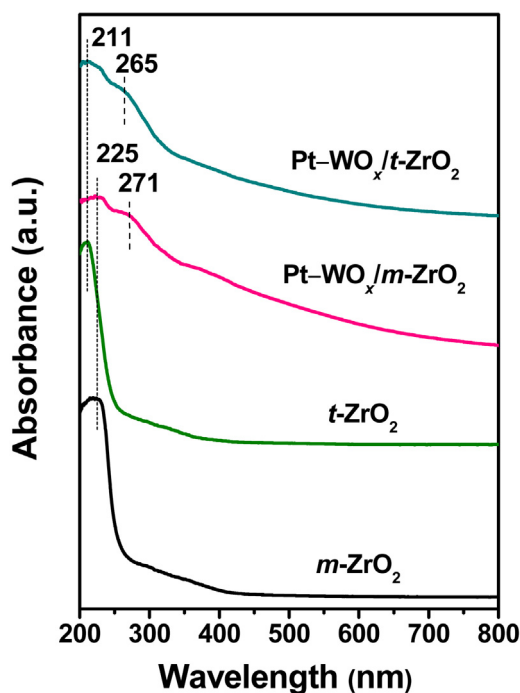


Fig. 4. The UV-vis DRS spectra of the as-synthesized $m\text{-ZrO}_2$, $t\text{-ZrO}_2$, and the $\text{Pt-WO}_x/m\text{-ZrO}_2$ and $\text{Pt-WO}_x/t\text{-ZrO}_2$ catalysts.

3.2.4. Identity of WO_x

Fig. 4 presents the UV-vis DRS spectra of the ZrO_2 supports and the $\text{Pt-WO}_x/\text{ZrO}_2$ catalysts. According to the spectra of the ZrO_2 supports, the band below 230 nm was due to charge transfer from the oxygen anions to the zirconium cations ($\text{O}^{2-} \rightarrow \text{Zr}^{4+}$) in ZrO_2 [40,41]. The additional band at around 270 nm for both $\text{Pt-WO}_x/\text{ZrO}_2$ catalysts may be assigned to the tungsten species in a distorted tetrahedral or an octahedral coordination environment [42].

The Raman spectra of the $\text{Pt-WO}_x/\text{ZrO}_2$ catalysts are presented in Fig. 2. The bands characteristic of HSiW at 995 and 974 cm^{-1} [43] were not visible due to the complete decomposition of HSiW after calcination at 723 K [44]. The band ascribable to the W–O–W stretching mode at about 830 cm^{-1} [45,46] was also unavailable, signifying that the WO_x species are monomeric rather than polymeric. Instead, there was a strong band at about 962 cm^{-1} that is attributable to the stretching mode of W=O in the highly dispersed WO_x species [47] in addition to a shoulder peak at about 922 cm^{-1} that is assigned to the bridging W–O–Zr bonds [36].

Fig. 5 shows the FTIR spectra of the $\text{Pt-WO}_x/\text{ZrO}_2$ catalysts. Entirely consistent with the Raman results, the bands characteristic of HSiW at 978, 915, 885, and 798 cm^{-1} [41,48] and the W–O–W asymmetric stretching vibration band at about 890 cm^{-1} [49] were also not resolved. On the other hand, the Zr–OH stretching vibration band at around 750 cm^{-1} that was originally quite strong on the as-synthesized ZrO_2 supports [16,50] was drastically attenuated on the $\text{Pt-WO}_x/\text{ZrO}_2$ catalysts, indicating the anchorage of Pt and WO_x on the ZrO_2 supports via the surface Zr–OH groups by forming the bridging Zr–O–Pt/W bonds.

3.2.5. Chemical state and surface composition

Fig. 6 presents the XPS spectra of the Pt 4f and W 4f levels of the $\text{Pt-WO}_x/\text{ZrO}_2$ catalysts; the fitting results are compiled in Table 2. Since the Pt 4f doublet overlaps with the W 5s signal, the latter was subtracted when fitting the Pt 4f spectra (Fig. 6a). The Pt 4f spectra were fitted into two doublets with the Pt 4f_{7/2} BEs of ca. 71.4 and 72.8 eV ascribable to Pt^0 and Pt^{2+} , respec-

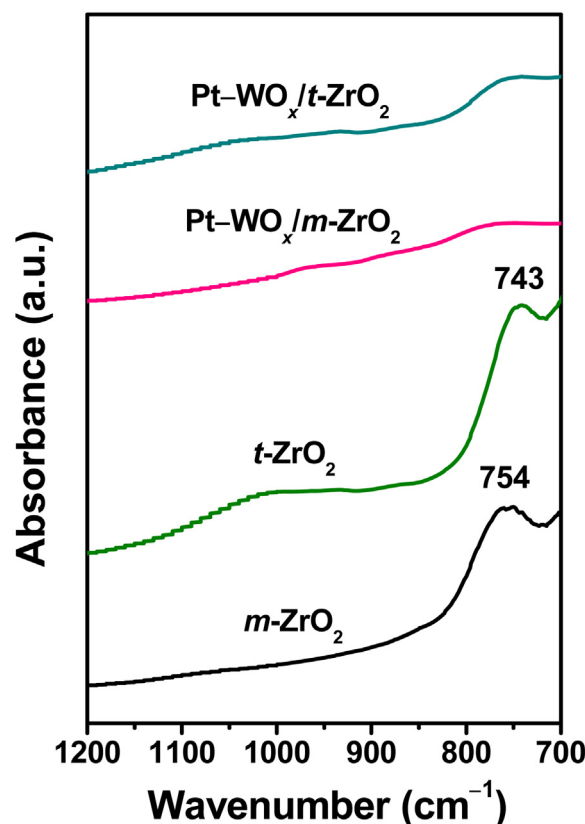


Fig. 5. The FTIR spectra of the as-synthesized $m\text{-ZrO}_2$, $t\text{-ZrO}_2$, and the $\text{Pt-WO}_x/m\text{-ZrO}_2$ and $\text{Pt-WO}_x/t\text{-ZrO}_2$ catalysts.

tively [51]. Despite of the identical Pt loadings, the surface Pt/Zr atomic ratio was substantially higher on the $\text{Pt-WO}_x/t\text{-ZrO}_2$ catalyst than on the $\text{Pt-WO}_x/m\text{-ZrO}_2$ catalyst. This finding complies with the CO chemisorption and HRTEM results that $t\text{-ZrO}_2$ afforded a better dispersion of Pt. In addition, the surface $\text{Pt}^{2+}/(\text{Pt}^0 + \text{Pt}^{2+})$ ratios on the $\text{Pt-WO}_x/m\text{-ZrO}_2$ catalyst and the $\text{Pt-WO}_x/t\text{-ZrO}_2$ catalyst were 0.04 and 0.06, respectively. Arribas et al. observed the Pt^{2+} species on the $\text{Pt/WO}_3\text{-ZrO}_2$ catalyst with highly dispersed Pt nanoparticles and interpreted as an indication of the strong interaction between Pt and the surface tungsten species [52]. Herein, we assume that such Pt^{2+} species are the Pt atoms at the periphery of the sub-nanosized Pt particles in direct contact with ZrO_2 and WO_x via the bridging Pt–O–Zr/W bonds, which is a common bonding configuration of metals on oxides [53–56]. Therefore, the $\text{Pt-WO}_x/t\text{-ZrO}_2$ catalyst with smaller Pt particles possesses more peripheral Pt–O–Zr/W bonds and hence larger surface $\text{Pt}^{2+}/(\text{Pt}^0 + \text{Pt}^{2+})$ ratio. Similarly, Campa et al. observed that for the Rh/ ZrO_2 catalysts, $t\text{-ZrO}_2$ could disperse Rh better than $m\text{-ZrO}_2$ [23]. They further observed that there was a higher population of the Rh sites in direct contact with $t\text{-ZrO}_2$, which reflects the occurrence of a stronger interaction of Rh with $t\text{-ZrO}_2$ that is conducive to the dispersion of Rh. The weaker interaction between metal and $m\text{-ZrO}_2$ may be attributed to the more covalent character of the Zr–O bond and more oxygen-defective structure of $m\text{-ZrO}_2$, which hinders electron transfer from metal to $m\text{-ZrO}_2$ and impedes the formation of the metal sites in direct contact with the support [23].

Fig. 6b displays the W 4f spectra of the $\text{Pt-WO}_x/\text{ZrO}_2$ catalysts. Aside from the Zr 4p doublet, there were two W 4f doublets with the W 4f_{7/2} BEs of ca. 35.6 and 34.9 eV ascribable to the W^{6+} and W^{5+} species, respectively [57]. There are two possible origins of the W^{5+} species. One is the partial reduction of the W^{6+} species in H_2 [58,59], and the other is the strong interaction between WO_x and ZrO_2 [60].

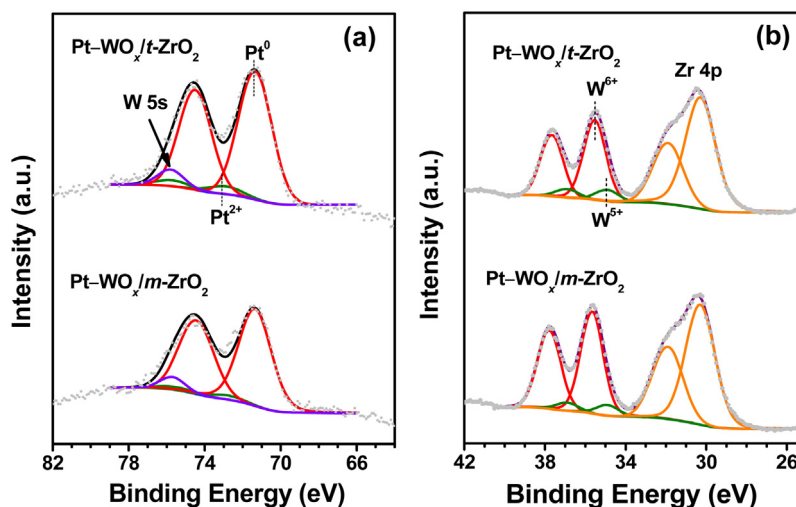


Fig. 6. (a) The Pt 4f and (b) W 4f spectra of the Pt-WO_x/m-ZrO₂ and Pt-WO_x/t-ZrO₂ catalysts.

Table 2

XPS fitting results of the Pt-WO_x/m-ZrO₂ and Pt-WO_x/t-ZrO₂ catalysts.

Catalyst	4f _{7/2} BE (eV)				Pt ²⁺ /(Pt ⁰ + Pt ²⁺) intensity ratio	W ⁵⁺ /(W ⁵⁺ + W ⁶⁺) intensity ratio	Pt/Zr (atom%)	W/Zr (atom%)
	Pt ²⁺	Pt ⁰	W ⁶⁺	W ⁵⁺				
Pt-WO _x /m-ZrO ₂	72.8	71.4	35.7	34.9	0.04	0.10	1.2	7.1
Pt-WO _x /t-ZrO ₂	72.9	71.4	35.6	34.9	0.06	0.12	1.8	7.0

As listed in Table 2, the surface W⁵⁺/(W⁵⁺ + W⁶⁺) ratio was slightly larger on the Pt-WO_x/t-ZrO₂ catalyst than on the Pt-WO_x/m-ZrO₂ catalyst, while the surface W/Zr ratios were essentially identical on both catalysts.

3.2.6. Acidic property

Fig. 7 displays the Py-IR spectra of the Pt-WO_x/ZrO₂ catalysts collected at 373 and 473 K, along with the spectra of the as-synthesized ZrO₂ supports for comparison. According to the literature [14], the bands at about 1448 and 1607 cm⁻¹ were due to pyridine coordinated to Lewis acid sites. The band at 1488 cm⁻¹ was attributed to a combination of pyridine on Lewis acid sites and Brønsted acid sites, while the band at around 1542 cm⁻¹ was typical for pyridine coordinated to Brønsted acid sites [61]. Although the Py-IR spectra of the as-synthesized m-ZrO₂ and t-ZrO₂ supports resembled each other in terms of shape and intensity, the spectra of the Pt-WO_x/ZrO₂ catalysts were obviously at variance. The intensities of the vibration bands on the Pt-WO_x/m-ZrO₂ catalyst were much weaker than those on the Pt-WO_x/t-ZrO₂ catalyst at both temperatures, reflecting that there were fewer and weaker acid sites on the former than on the latter despite of the identical Pt and WO_x loadings.

On the basis of Fig. 7, the amounts of Lewis and Brønsted acid sites on the as-synthesized ZrO₂ supports and the Pt-WO_x/ZrO₂ catalysts were quantified respectively from the integral intensities of the bands at 1448 and 1542 cm⁻¹ and their molar extinction coefficients. Table 3 shows that the total amounts of the acid sites (*n*_{L+B}) on the as-synthesized m-ZrO₂ and t-ZrO₂ supports were similar. However, loading Pt and WO_x on m-ZrO₂ diminished both Lewis and Brønsted acid sites, while loading Pt and WO_x on t-ZrO₂ increased both Lewis acid sites and Brønsted acid sites, resulting in the *n*_{L+B} on the Pt-WO_x/m-ZrO₂ catalyst only about one half of that on the Pt-WO_x/t-ZrO₂ catalyst. Moreover, there were more Lewis acid sites than Brønsted acid sites on the Pt-WO_x/m-ZrO₂ catalyst, while a reversed sequence was found on the Pt-WO_x/t-ZrO₂ catalyst.

3.3. Catalytic results in glycerol hydrogenolysis

3.3.1. Activity and selectivity

The catalytic results of glycerol hydrogenolysis over the Pt-WO_x/ZrO₂ catalysts at 413 K and 8.0 MPa of H₂ are summarized in Table 4. It was found that the CTL was 33.8% on the Pt-WO_x/m-ZrO₂ catalyst, which was only about one half of the CTL (76.2%) on the Pt-WO_x/t-ZrO₂ catalyst under identical reaction conditions. The 1,3-PDO selectivity was 28.1% on the Pt-WO_x/m-ZrO₂ catalyst, while it amounted to 64.8% on the Pt-WO_x/t-ZrO₂ catalyst. As a result, the yield of 1,3-PDO was 9.5% on the Pt-WO_x/m-ZrO₂ catalyst, while it was as high as 49.4% on the Pt-WO_x/t-ZrO₂ catalyst, which clearly demonstrates the superiority of t-ZrO₂ to m-ZrO₂ as the support for Pt-WO_x in glycerol hydrogenolysis to 1,3-PDO. It should be mentioned that the yield of 1,3-PDO on the Pt-WO_x/t-ZrO₂ catalyst is higher than those reported previously on the Pt/WO₃/ZrO₂ catalysts [11–13], the Pt-H₄SiW₁₂O₄₀/ZrO₂ catalysts without and with Li modification [14,15], and the 5Pt/WO_x/ZrSi catalyst [16].

As to the STY of 1,3-PDO, it was as low as 0.98 g g_{Pt}⁻¹ h⁻¹ on the Pt-WO_x/m-ZrO₂ catalyst. In sharp contrast, it was 5.10 g g_{Pt}⁻¹ h⁻¹ on the Pt-WO_x/t-ZrO₂ catalyst, which, as far as we are aware of, is the highest value ever reported on the Pt-WO_x-based catalysts in glycerol hydrogenolysis to 1,3-PDO (Table S1). Recently, Wang et al. reported a record-high STY of 1,3-PDO of 3.78 g g_{Pt}⁻¹ h⁻¹ among the Pt-WO_x-based catalysts over the mesoporous WO_x-supported single/pseudo-single atom Pt catalyst (Pt/meso-WO_x) at 433 K [62]. At 413 K, the STY of 1,3-PDO on the Pt/meso-WO_x catalyst was 1.96 g g_{Pt}⁻¹ h⁻¹. Over the Pt/WO_x/AlOOH catalyst displaying the highest 1,3-PDO yield of ca. 66% to date, the STY of 1,3-PDO was 2.32 g g_{Pt}⁻¹ h⁻¹ at 453 K [63]. When lowering the temperature to 413 K, it concomitantly decreased to 0.45 g g_{Pt}⁻¹ h⁻¹, which is about one order of magnitude lower than the STY of 1,3-PDO over the Pt-WO_x/t-ZrO₂ catalyst at the same reaction temperature.

In the open literature, the Ir-ReO_x/SiO₂ catalyst exhibited the highest STY of 1,3-PDO in glycerol hydrogenolysis. Nakagawa et al.

Table 3Acidic properties of the as-synthesized m -ZrO₂, t -ZrO₂, and the Pt-WO_x/ m -ZrO₂ and Pt-WO_x/ t -ZrO₂ catalysts.

Sample	n_L (mmol g _{cat} ⁻¹)		n_B (mmol g _{cat} ⁻¹)		n_{L+B} (mmol g _{cat} ⁻¹)		n_B/n_{L+B}	
	373 K	473 K	373 K	473 K	373 K	473 K	373 K	473 K
m -ZrO ₂	0.21	0.093	0.12	0.080	0.33	0.17	0.37	0.46
t -ZrO ₂	0.18	0.085	0.13	0.086	0.31	0.17	0.43	0.50
Pt-WO _x / m -ZrO ₂	0.096	0.066	0.077	0.039	0.17	0.11	0.45	0.37
Pt-WO _x / t -ZrO ₂	0.18	0.10	0.20	0.11	0.38	0.21	0.52	0.51

Table 4The catalytic results over the Pt-WO_x/ m -ZrO₂, Pt-WO_x/ t -ZrO₂, Pt/ t -ZrO₂, and WO_x/ t -ZrO₂ catalysts in the hydrogenolysis of glycerol^a.

Catalyst	Conversion (%)	CTL (%)	Sel. (C% in liquid products)					Yield _{1,3-PDO} (%)	STY (g g _{Pt} ⁻¹ h ⁻¹)
			1,3-PDO	1,2-PDO	1-PrOH	2-PrOH	Others		
Pt-WO _x / m -ZrO ₂	36.4	33.8	28.1	2.3	31.0	32.3	6.3	9.5	0.98
Pt-WO _x / t -ZrO ₂	78.3	76.2	64.8	1.6	27.5	6.0	trace	49.4	5.10
Pt/ t -ZrO ₂	0.85	0.81	2.8	28.7	57.3	11.2	trace	trace	–
WO _x / t -ZrO ₂	1.9	1.8	4.9	0.7	37.5	56.7	trace	trace	–

^a Reaction conditions: 100 mg of catalyst, 2.0 g of 30 wt% glycerol aqueous solution, temperature of 413 K, H₂ pressure of 8.0 MPa, stirring rate of 500 rpm, and reaction time of 24 h.

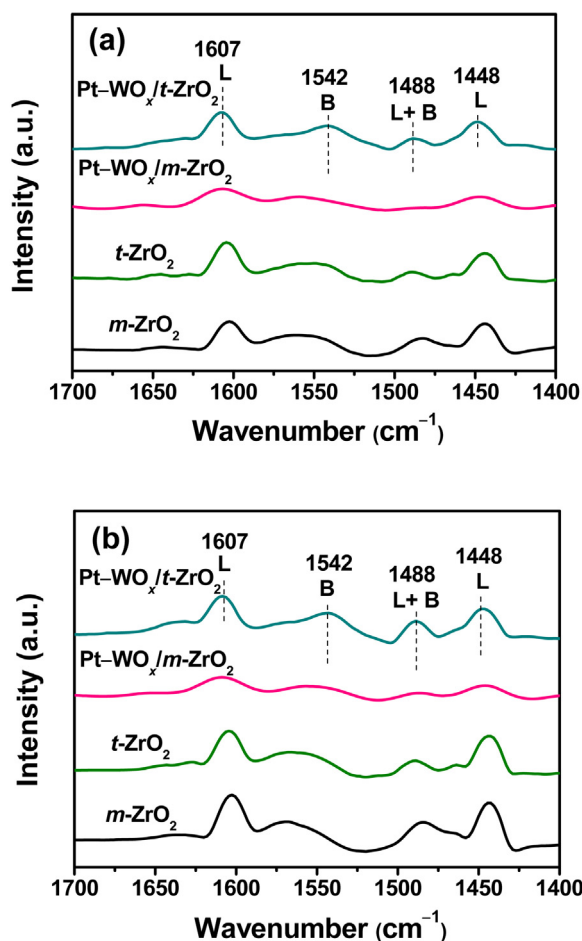


Fig. 7. The Py-IR spectra of the Pt-WO_x/ m -ZrO₂ and Pt-WO_x/ t -ZrO₂ catalysts acquired at (a) 373 K and (b) 473 K. The spectra of the as-synthesized m -ZrO₂ and t -ZrO₂ are also presented for comparison.

reported the STY of 1,3-PDO of as high as 14.25 g g_{Pt}⁻¹ h⁻¹ over the Ir-ReO_x/SiO₂ catalyst at 393 K [64]. However, aside from the defect that ReO_x is inclined to dissolve in water [65], the environmentally unfriendly H₂SO₄ was added to promote the reaction. When H₂SO₄ was replaced by ZSM-5, it decreased to 6.03 g g_{Pt}⁻¹ h⁻¹ [66], which is comparable to the value over the Pt-WO_x/ t -ZrO₂ catalyst.

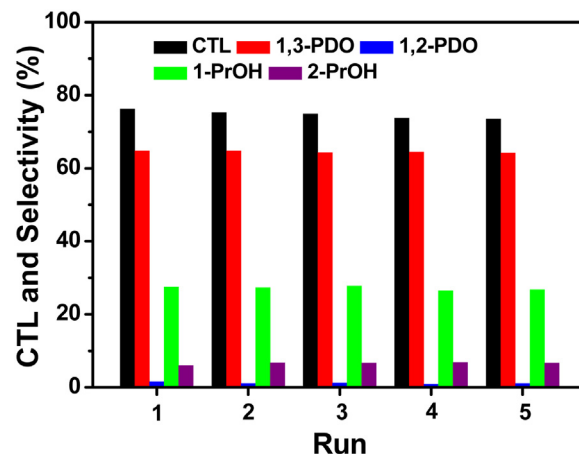


Fig. 8. The CTL and product distribution in glycerol hydrogenolysis over the Pt-WO_x/ t -ZrO₂ catalyst in five successive runs. Reaction conditions: 100 mg of catalyst, 2.0 g of 30 wt% glycerol aqueous solution, temperature of 413 K, H₂ pressure of 8.0 MPa, stirring rate of 500 rpm, and reaction time of 24 h.

3.3.2. Stability

Since the Pt-WO_x/ t -ZrO₂ catalyst exhibited excellent catalytic performance in glycerol hydrogenolysis to 1,3-PDO, its stability was examined and illustrated in Fig. 8. It is remarkable that the CTL decreased negligibly from 76.2% in the first run to 73.5% in the fifth run. The ~0.54% per run CTL drop is more likely caused by catalyst loss due to attrition in stirred liquid-phase reaction and repetitive catalyst recovery than by the irreversible degradation of the catalyst. This interpretation is supported by the essentially unaltered selectivities to 1,3-PDO and other hydrogenolysis products in five successive runs also depicted in Fig. 8. Therefore, the excellent activity, high 1,3-PDO selectivity, and remarkable robustness of the Pt-WO_x/ t -ZrO₂ catalyst render it a highly promising candidate for practical applications. The Pt-WO_x/ m -ZrO₂ catalyst was also relatively stable in repeated runs (Fig. S3), despite of its much lower CTL and 1,3-PDO selectivity.

4. Discussion

In glycerol hydrogenolysis, the Pt-WO_x/ t -ZrO₂ catalyst exhibited much higher CTL as well as selectivity, yield, and STY of 1,3-PDO than the Pt-WO_x/ m -ZrO₂ catalyst. Over the supported Pt-H₄SiW₁₂O₄₀ catalysts, Zhu et al. demonstrated that smaller Pt

particle size is conducive to a higher catalytic activity in glycerol hydrogenolysis [67], which may account for the higher CTL over the Pt–WO_x/t-ZrO₂ catalyst with smaller Pt particle size than the Pt–WO_x/m-ZrO₂ catalyst, as revealed by CO chemisorption, HRTEM, and HAADF–STEM. However, due to the high complexity of the mechanism of glycerol hydrogenolysis [6,10,15,68–70], the effect of the particle size of Pt on the catalytic activity is far more delicate. In a control experiment, we evaluated the Pt/t-ZrO₂ catalyst in glycerol hydrogenolysis. Under the same reaction conditions, the CTL was negligible (0.81%) in the absence of WO_x (Table 4). In another control experiment, we prepared the WO_x/t-ZrO₂ catalyst following the procedures of the Pt–WO_x/t-ZrO₂ catalyst but skipping the steps for the loading of Pt. Under the same reaction conditions, the CTL was only 1.8% in the absence of Pt (Table 4). Therefore, it is more justified that it is the interplay between Pt, WO_x, and t-ZrO₂ that boosts the activity of glycerol hydrogenolysis over the Pt–WO_x/t-ZrO₂ catalyst, as will be elaborated below.

In fact, tungstated zirconia (WO_x/ZrO₂) and platinum-on-tungstated zirconia (Pt/WO_x/ZrO₂) have been known as excellent solid acid catalysts in alkane isomerization, aromatic acrylation, alkylation, alcohol dehydration, and so on [71,72]. It was identified that the crystal phases of ZrO₂ are critical to their acid properties, with the t-ZrO₂-supported WO_x or Pt–WO_x being more acidic than the m-ZrO₂-supported counterparts [34,73–75], though the underlying chemistry remains unclear. Coincident with the literature works, Table 3 shows that the n_{L+B} on the Pt–WO_x/t-ZrO₂ catalyst was about two folds of that on the Pt–WO_x/m-ZrO₂ catalyst. Furthermore, the n_B/n_{L+B} ratio on the Pt–WO_x/t-ZrO₂ catalyst was higher than that on the Pt–WO_x/m-ZrO₂ catalyst. When elevating the temperature from 373 K to 473 K, the n_B/n_{L+B} ratio retained at ~0.51 on the Pt–WO_x/t-ZrO₂ catalyst, while it decreased noticeably from 0.45 to 0.37 on the Pt–WO_x/m-ZrO₂ catalyst. These facts manifest that Brønsted acid sites are not only more abundant but also more strongly bonded on the Pt–WO_x/t-ZrO₂ catalyst than on the Pt–WO_x/m-ZrO₂ catalyst.

The type and amount of the acid sites have been found to exert a decisive effect on the product distribution in glycerol hydrogenolysis. In general, Lewis acid sites favor the formation of the less desirable 1,2-PDO [76,77], whereas Brønsted acid sites favor the formation of 1,3-PDO [59,78]. In particular, Zhu et al. established a linear relationship between the yield of 1,2-PDO (inclusive of the derived propanols) and the concentration of Lewis acid sites [14] and a linear relationship between the yield of 1,3-PDO and the concentration of Brønsted acid sites on catalysts containing Pt and heteropolyacids [14,15]. There are two prevailing mechanisms addressing the role of Brønsted acid sites in glycerol hydrogenolysis to 1,3-PDO over the Pt–WO_x-based catalysts. One is direct protonation of the secondary hydroxyl group of glycerol, which accelerates the depletion of this group [13,14]. The other is the etherification of glycerol with the Brønsted acid sites (M–OH) on the catalyst to form the M–O–CH₂CH(OH)CH₂OH surface species, which is advantageous to the depletion of the secondary hydroxyl group of glycerol in following step [10,62,70,79]. Hence, irrespective of the reaction mechanisms, the production of 1,3-PDO should be a more preferred reaction pathway on the Pt–WO_x/t-ZrO₂ catalyst with more Brønsted acid sites. Table 4 shows that the selectivities to 1,2-PDO and its derivative 2-PrOH on the Pt–WO_x/m-ZrO₂ catalyst with more Lewis acid sites were much higher than those on the Pt–WO_x/t-ZrO₂ catalyst, additionally substantiating the sharply different roles of Lewis acid sites and Brønsted acid sites in selectivity modulation in glycerol hydrogenolysis.

In these two mechanisms, Pt plays the role of dissociating H₂ to H atoms, which spillover to WO_x and participate in the hydrogenation of the reaction intermediate to 1,3-PDO and the recovery of Brønsted acid sites [10,13,14,62,80]. Since the dissociation of H₂ on Pt is essentially barrierless [81–83], it should not be the

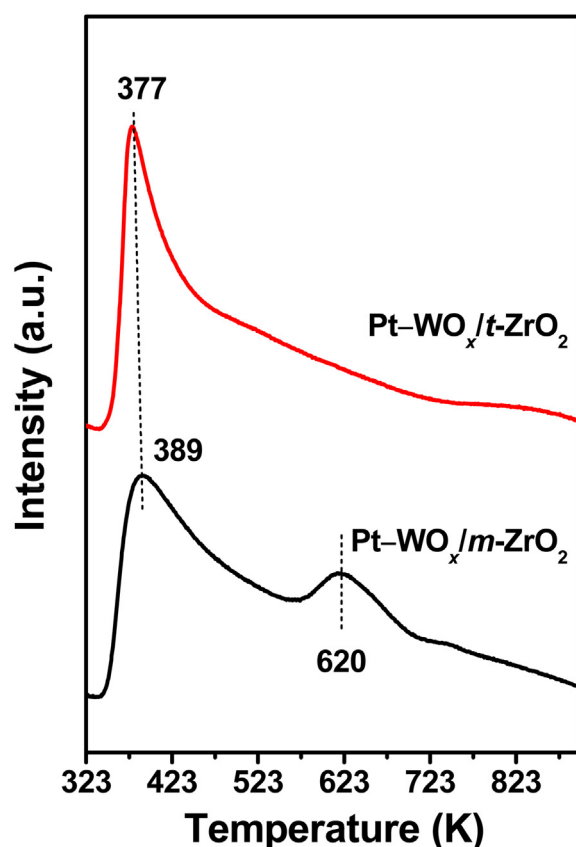


Fig. 9. The H₂-TPD profiles of the Pt–WO_x/m-ZrO₂ and Pt–WO_x/t-ZrO₂ catalysts.

rate-determining step in the present reaction. Instead, Hattori and co-workers found that the spillover of H atoms onto the WO₃–ZrO₂ surface was the rate-determining step on the Pt/WO₃–ZrO₂ catalyst [84]. On the other hand, Takasu et al. have shown that the activation energy for the desorption of hydrogen increased proportionally with the enlargement of the Pt particle size [85]. This finding agrees well with the report of Yang and co-workers that smaller Pt sizes were needed for hydrogen spillover on the Pt-doped metal–organic framework IRMOF-8 materials [86], considering that more weakly bonded H atoms on smaller Pt particles would allow for easier hydrogen spillover. To gain an insight into the effect of the particle size of Pt on the binding strength of H atoms on the Pt–WO_x/ZrO₂ catalysts, the H₂-TPD characterization was carried out. Fig. 9 shows that there was a strong peak at 389 K and a shoulder peak at 620 K for the Pt–WO_x/m-ZrO₂ catalyst, while there was only one strong desorption peak at 377 K for the Pt–WO_x/t-ZrO₂ catalyst. The high-temperature peak is ascribed to hydrogen on m-ZrO₂, either directly chemisorbed or spillover from Pt [87], since the Pt/m-ZrO₂ catalyst also displayed a peak at similar temperature, while the Pt/t-ZrO₂ catalyst did not (Fig. S4). It is justified that the high bonding strength of hydrogen on m-ZrO₂ would not facilitate hydrogen spillover from m-ZrO₂ to WO_x. The low-temperature peak is assigned to the desorption of hydrogen from metallic Pt [88,89], which directly evidences that H atoms are less strongly bound on the Pt particles over the Pt–WO_x/t-ZrO₂ catalyst with smaller size. Consequently, the enhanced hydrogen spillover from Pt to WO_x on the Pt–WO_x/t-ZrO₂ catalyst makes it easier to hydrogenate the intermediate to 1,3-PDO and restore Brønsted acid sites. This interpretation complies with the conclusion drawn from a recent mechanistic study based on *in situ* and *ex situ* attenuated total reflection infrared spectroscopy that the high availability of Brønsted acid sites and the fast hydrogenation of the intermediate

to 1,3-PDO seem to be the key parameters to boost the formation of 1,3-PDO [79].

5. Conclusions

We unveiled that the structural characteristics and catalytic performances of the Pt–WO_x/ZrO₂ catalysts rely decisively on the crystal phases of ZrO₂. Tetrahedral ZrO₂ is more powerful than monoclinic ZrO₂ in dispersing smaller Pt particles and generating more and stronger Brønsted acid sites in the presence of WO_x. In glycerol hydrogenolysis to 1,3-PDO, the Pt–WO_x/t-ZrO₂ catalyst was far more active and selective than the Pt–WO_x/m-ZrO₂ catalyst under the same reaction conditions. The Pt–WO_x/t-ZrO₂ catalyst also displayed remarkable stability in repeated catalytic runs. The better interplay between smaller Pt particles and higher population of Brønsted acid sites is suggested to be responsible for the superior catalytic performance of the Pt–WO_x/t-ZrO₂ catalyst. This work clearly demonstrates the importance of using an appropriate crystallographic form of the catalyst support in the highly challenging but industrially and environmentally significant reaction of glycerol hydrogenolysis to 1,3-PDO.

Acknowledgements

This work was supported by the National Basic Research Program of China (2016YFB0301602), the National Natural Science Foundation of China (21373055), and the Science and Technology Commission of Shanghai Municipality (08DZ2270500).

Appendix A. Supplementary data

Supplementary data associated with this article can be found, in the online version, at <http://dx.doi.org/10.1016/j.apcatb.2017.06.011>.

References

- [1] C.H. Zhou, J.N. Beltrami, Y.X. Fan, G.Q. Lu, *Chem. Soc. Rev.* 37 (2008) 527–549.
- [2] B. Katryniok, S. Paul, V. Belliere-Baca, P. Rey, F. Dumeignil, *Green Chem.* 12 (2010) 2079–2098.
- [3] D.L. Sun, Y. Yamada, S. Sato, W. Ueda, *Appl. Catal. B* 193 (2016) 75–92.
- [4] N. Benipal, J. Qi, Q. Liu, W.Z. Li, *Appl. Catal. B* 210 (2017) 121–130.
- [5] Y. Nakagawa, M. Tamura, K. Tomishige, *J. Mater. Chem. A* 2 (2014) 6688–6702.
- [6] Y.L. Wang, J.X. Zhou, X.W. Guo, *RSC Adv.* 5 (2015) 74611–74628.
- [7] R. Mane, S. Patil, M. Shirai, S. Rayalu, C. Rode, *Appl. Catal. B* 204 (2017) 134–146.
- [8] J. Chaminand, L. Djakovitch, P. Gallezot, P. Marion, C. Pinel, C. Rosier, *Green Chem.* 6 (2004) 359–361.
- [9] A. Zeng, H. Biebl, *Adv. Biochem. Eng. Biotechnol.* 74 (2002) 237–257.
- [10] S. García-Fernández, I. Gandarias, J. Requies, M.B. Güemez, S. Bennici, A. Auroux, P.L. Arias, *J. Catal.* 323 (2015) 65–75.
- [11] T. Kurosaka, H. Maruyama, I. Naribayashi, Y. Sasaki, *Catal. Commun.* 9 (2008) 1360–1363.
- [12] L.F. Gong, Y. Lü, Y.J. Ding, R.H. Lin, J.W. Li, W.D. Dong, T. Wang, W.M. Chen, *Chin. J. Catal.* 30 (2009) 1189–1191.
- [13] L.Z. Qin, M.J. Song, C.L. Chen, *Green Chem.* 12 (2010) 1466–1472.
- [14] S.H. Zhu, Y.N. Qiu, Y.L. Zhu, S.L. Hao, H.Y. Zheng, Y.W. Li, *Catal. Today* 212 (2013) 120–126.
- [15] S.H. Zhu, X.Q. Gao, Y.L. Zhu, Y.F. Zhu, X.M. Xiang, C.X. Hu, Y.W. Li, *Appl. Catal. B* 140–141 (2013) 60–67.
- [16] S.H. Zhu, X.Q. Gao, Y.L. Zhu, J.L. Cui, H.Y. Zheng, Y.W. Li, *Appl. Catal. B* 158–159 (2014) 391–399.
- [17] S. Shukla, S. Seal, *J. Phys. Chem. B* 108 (2004) 3395–3399.
- [18] W. Stichert, F. Schüth, S. Kuba, H. Knözinger, *J. Catal.* 198 (2001) 277–285.
- [19] D.P. He, Y.J. Ding, H.Y. Luo, C. Li, *J. Mol. Catal. A* 208 (2004) 267–271.
- [20] Z.H. Ma, C. Yang, W. Wei, W.H. Li, Y.H. Sun, *J. Mol. Catal. A* 231 (2005) 75–81.
- [21] G.B. Zhou, J.L. Liu, X.H. Tan, Y. Pei, M.H. Qiao, K.N. Fan, B.N. Zong, *Ind. Eng. Chem. Res.* 51 (2012) 12205–12213.
- [22] H. Xie, J.L. Lu, M. Shekhar, J.W. Elam, W.N. Delgass, F.H. Ribeiro, E. Weitz, K.R. Poepelmeier, *ACS Catal.* 3 (2013) 61–73.
- [23] M.C. Campa, G. Ferraris, D. Gazzoli, I. Pettiti, D. Pietrogiaconi, *Appl. Catal. B* 142–143 (2013) 423–431.
- [24] J. Li, J.L. Chen, W. Song, J.L. Liu, W.J. Shen, *Appl. Catal. A* 334 (2008) 321–329.
- [25] K.V.R. Chary, K. Ramesh, D. Naresh, P.V.R. Rao, A.R. Rao, V.V. Rao, *Catal. Today* 141 (2009) 187–194.
- [26] W.Z. Li, H. Huang, H.J. Li, W. Zhang, H.C. Liu, *Langmuir* 24 (2008) 8358–8366.
- [27] K.T. Jung, A.T. Bell, *J. Mol. Catal. A* 163 (2000) 27–42.
- [28] A.M. Karim, V. Prasad, G. Mpourmpakis, W.W. Loneragan, A.I. Frenkel, J.G. Chen, D.G. Vlachos, *J. Am. Chem. Soc.* 131 (2009) 12230–12239.
- [29] Y. Izutsu, Y. Oku, Y. Hidaka, N. Kanaya, Y. Nakajima, J. Fukuroi, K. Yoshida, Y. Sasaki, Y. Sekine, M.J. Matsukata, *J. Phys. Chem. C* 118 (2014) 10746–10753.
- [30] G.B. Zhou, Y. Pei, Z. Jiang, K.N. Fan, M.H. Qiao, B. Sun, B.N. Zong, *J. Catal.* 311 (2014) 393–403.
- [31] C.A. Emeis, *J. Catal.* 141 (1993) 347–354.
- [32] S. Kongjao, S. Damronglerd, M. Hunsom, *Korean J. Chem. Eng.* 27 (2010) 944–949.
- [33] A. Punnoose, M.S. Seehra, I. Wender, *Fuel Process. Technol.* 74 (2001) 33–47.
- [34] B.Y. Zhao, X.P. Xu, J.M. Gao, Q. Fu, Y.Q. Tang, *J. Raman Spectrosc.* 27 (1996) 549–554.
- [35] M.D. Rhodes, A.T. Bell, *J. Catal.* 233 (2005) 198–209.
- [36] E.I. Ross-Medgaarden, W.V. Knowles, T. Kim, M.S. Wong, W. Zhou, C.J. Kiely, I.E. Wachs, *J. Catal.* 256 (2008) 108–125.
- [37] H.J. Stolz, G. Abstreiter, *J. Vac. Sci. Technol.* 19 (1981) 380–382.
- [38] D.G. Barton, M. Shtein, R.D. Wilson, S.L. Soled, E. Iglesia, *J. Phys. Chem. B* 103 (1999) 630–640.
- [39] W. Zhou, E.I. Ross-Medgaarden, W.V. Knowles, M.S. Wong, I.E. Wachs, C.J. Kiely, *Nat. Chem.* 1 (2009) 722–728.
- [40] D. Ciuparu, A. Ensueque, G. Shafiev, F. Bozon-Verduraz, *J. Mater. Sci. Lett.* 19 (2000) 931–933.
- [41] K.M. Parida, S. Mallick, *J. Mater. Chem. A* 275 (2007) 77–83.
- [42] J.C. Hu, Y.D. Wang, L.F. Chen, *Microporous Mesoporous Mat.* 93 (2006) 158–163.
- [43] H. Atia, U. Armbruster, A. Martin, *J. Catal.* 258 (2008) 71–82.
- [44] I.V. Kozhevnikov, *J. Mater. Chem. A* 262 (2007) 86–92.
- [45] M. Scheithauer, R.K. Grasselli, H. Knözinger, *Langmuir* 14 (1998) 3019–3029.
- [46] Z.C. Si, D. Weng, X.D. Wu, Y. Jiang, B. Wang, *Catal. Sci. Technol.* 1 (2011) 453–461.
- [47] M.N. Taylor, W. Zhou, T. Garcia, B. Solsona, A.F. Carley, C.J. Kiely, S.H. Taylor, *J. Catal.* 285 (2012) 103–114.
- [48] N. Bhatt, A. Patel, *J. Mater. Chem. A* 238 (2005) 223–228.
- [49] S. Ghosh, S.S. Acharyya, T. Sasaki, R. Bal, *Green Chem.* 17 (2015) 1867–1876.
- [50] J. Liu, S.G. Bian, M. Xiao, S.J. Wang, Y.Z. Meng, *Catal. Lett.* 131 (2009) 305–311.
- [51] J.F. Moulder, W.F. Stickle, P.E. Sobol, K.D. Bomben, *Handbook of X-ray Photoelectron Spectroscopy*, in: J. Chastain (Ed.), Perkin-Elmer, Eden Prairie, MN, 1992.
- [52] M. Arribas, F. Márquez, A. Martínez, *J. Catal.* 190 (2000) 309–319.
- [53] C. Jung, R. Ishimoto, H. Tsuboi, M. Koyama, A. Endou, M. Kubo, C.A. Del Carpio, A. Miyamoto, *Appl. Catal. A* 305 (2006) 102–109.
- [54] C.H. Hu, C. Chizallet, C. Mager-Maury, M. Corral-Valero, P. Sautet, H. Toulhoat, P. Raybaud, *J. Catal.* 274 (2010) 99–110.
- [55] M. Hatanaka, N. Takahashi, T. Tanabe, Y. Nagai, K. Dohmae, Y. Aoki, T. Yoshida, H. Shinjoh, *Appl. Catal. B* 99 (2010) 336–342.
- [56] P.X. Liu, Y. Zhao, R.X. Qin, S.G. Mo, G.X. Chen, L. Gu, D.M. Chevrier, P. Zhang, Q. Guo, D.D. Zang, B.H. Wu, G. Fu, N.F. Zheng, *Science* 352 (2016) 797–801.
- [57] Y.H. Zhang, X.C. Zhao, Y. Wang, L.K. Zhou, J.Y. Zhang, J. Wang, A.Q. Wang, T. Zhang, *J. Mater. Chem. A* 1 (2013) 3724–3732.
- [58] T. Baba, Y. Hasada, M. Nomura, Y. Ohno, Y. Ono, *J. Mol. Catal. A* 114 (1996) 247–255.
- [59] L.F. Gong, Y. Lü, Y.J. Ding, R.H. Lin, J.W. Li, W.D. Dong, T. Wang, W.M. Chen, *Appl. Catal. A* 390 (2010) 119–126.
- [60] F.J. Berry, G.R. Derrick, J.F. Marco, M. Mortimer, *Mater. Chem. Phys.* 114 (2009) 1000–1003.
- [61] P. Lauriol-Garbey, G. Postole, S. Lorient, A. Auroux, V. Belliere-Baca, P. Rey, J.M. Millet, *Appl. Catal. B* 106 (2011) 94–102.
- [62] J. Wang, X.C. Zhao, N. Lei, L. Li, L.L. Zhang, S.T. Xu, S. Miao, X.L. Pan, A.Q. Wang, T. Zhang, *ChemSusChem* 9 (2016) 784–790.
- [63] R. Arundhati, T. Mizugaki, T. Mitsudome, K. Jitsukawa, K. Kaneda, *ChemSusChem* 6 (2013) 1345–1347.
- [64] Y. Nakagawa, Y. Shinmi, S. Koso, K. Tomishige, *J. Catal.* 272 (2010) 191–194.
- [65] M. Chia, Y.J. Pagán-Torres, D. Hibbitts, Q.H. Tan, H.N. Pham, A.K. Datye, M. Neurock, R.J. Davis, J.A. Dumesic, *J. Am. Chem. Soc.* 133 (2011) 12675–12689.
- [66] Y. Nakagawa, X.H. Ning, Y. Amada, K. Tomishige, *Appl. Catal. A* 433–434 (2012) 128–134.
- [67] S.H. Zhu, Y.L. Zhu, S.L. Hao, H.Y. Zheng, T. Mo, Y.W. Li, *Green Chem.* 14 (2012) 2607–2616.
- [68] E.P. Maris, R.J. Davis, *J. Catal.* 249 (2007) 328–337.
- [69] Y. Shinmi, S. Koso, T. Kubota, Y. Nakagawa, K. Tomishige, *Appl. Catal. B* 94 (2010) 318–326.
- [70] T. Mizugaki, T. Yamakawa, R. Arundhati, T. Mitsudome, K. Jitsukawa, K. Kaneda, *Chem. Lett.* 41 (2012) 1720–1722.
- [71] N. Soultanidis, W. Zhou, A.C. Psarras, A.J. Gonzalez, E.F. Iliopoulou, C.J. Kiely, I.E. Wachs, M.S. Wong, *J. Am. Chem. Soc.* 132 (2010) 13462–13471.
- [72] H. Hattori, Y. Ono, *Solid Acid Catalysis-From Fundamentals to Applications*, Pan Stanford Publishing, 2015, pp. 271–282.
- [73] W.J. Ji, J.Q. Hu, Y. Chen, *Catal. Lett.* 53 (1998) 15–21.
- [74] J.C. Yori, J.M. Parera, *Catal. Lett.* 65 (2000) 205–208.
- [75] T. Yamamoto, A. Teramachi, A. Orita, A. Kurimoto, T. Motoi, T. Tanaka, *J. Phys. Chem. C* 120 (2016) 19705–19713.

- [76] A. Alhanash, E.F. Kozhevnikova, I.V. Kozhevnikov, *Appl. Catal. A* 378 (2010) 11–18.
- [77] Y.T. Kim, K.D. Jung, E.D. Park, *Appl. Catal. B* 107 (2011) 177–187.
- [78] J. Oh, S. Dash, H. Lee, *Green Chem.* 13 (2011) 2004–2007.
- [79] S. García-Fernández, I. Gandarias, J. Reques, F. Soulimani, P.L. Arias, B.M. Weckhuysen, *Appl. Catal. B* 204 (2017) 260–272.
- [80] D.G. Barton, S.L. Soled, G.D. Meitzner, G.A. Fuentes, E. Iglesia, *J. Catal.* 181 (1999) 57–72.
- [81] Q. Cui, D.G. Musaev, J. Morokuma, *J. Chem. Phys.* 108 (1998) 8418–8428.
- [82] C.G. Zhou, J.P. Wu, A.H. Nie, R.C. Forrey, A. Tachibana, H.S. Cheng, *J. Phys. Chem. C* 111 (2007) 12773–12778.
- [83] S.K. Ignatov, A.I. Okhapkin, O.B. Gadzhiev, A.G. Razuvaev, S. Kunz, M. Bäumer, *J. Phys. Chem. C* 120 (2016) 18570–18587.
- [84] S. Triwahyono, T. Yamada, H. Hattori, *Appl. Catal. A* 250 (2003) 65–73.
- [85] Y. Takasu, M. Teramoto, Y. Matsuda, *J. Chem. Soc. Chem. Commun.* (1983) 1329–1330.
- [86] L.F. Wang, N.R. Stuckert, H. Chen, R.T. Yang, *J. Phys. Chem. C* 115 (2011) 4793–4799.
- [87] D.L. Hoang, H. Berndt, H. Lieske, *Catal. Lett.* 31 (1995) 165–172.
- [88] D.L. Hoang, H. Lieske, *Catal. Lett.* 27 (1994) 33–42.
- [89] F. Lai, D.W. Kim, O.S. Alexeev, G.W. Graham, M. Shelef, B.C. Gates, *Phys. Chem. Chem. Phys.* 2 (2000) 1997–2003.